IT ISSN 0391 - 9838

GEOGRAFIA FISICA e DINAMICA QUATERNARIA

An international Journal published under the auspices of the
Rivista internazionale pubblicata sotto gli auspici di

Associazione Italiana di Geografia Fisica e Geomorfologia
and (e) Consiglio Nazionale delle Ricerche (CNR)

recognized by the (*riconosciuta da*)

International Association of Geomorphologists (IAG)

volume 43 (2)
2020

COMITATO GLACIOLOGICO ITALIANO - TORINO
2020

Bollettino del Comitato Glaciologico Italiano - ser. 3

GEOGRAFIA FISICA E DINAMICA QUATERNARIA

A journal published by the Comitato Glaciologico Italiano, under the auspices of the Associazione Italiana di Geografia Fisica e Geomorfologia and the Consiglio Nazionale delle Ricerche of Italy. Founded in 1978, it is the continuation of the «Bollettino del Comitato Glaciologico Italiano». It publishes original papers, short communications, news and book reviews of Physical Geography, Glaciology, Geomorphology and Quaternary Geology. The journal furthermore publishes the annual reports on italian glaciers, the official transactions of the Comitato Glaciologico Italiano and the Newsletters of the Intemational Association of Geomorphologists. Special issues, named «Geografia Fisica e Dinamica Quaternaria - Supplementi», collecting papers on specific themes, proceedings of meetings or symposia, regional studies, are also published, starting from 1988. The language of the journal is English, but papers can be written in other main scientific languages.

Rivista edita dal Comitato Glaciologico Italiano, sotto gli auspici dell'Associazione Italiana di Geografia Fisica e Geomorfologia e del Consiglio Nazionale delle Ricerche. Fondata nel 1978, è la continuazione del «Bollettino del Comitato Glaciologico Italiano». La rivista pubblica memorie e note originali, recensioni, corrispondenze e notiziari di Geografia Fisica, Glaciologia, Geomorfologia e Geologia del Quaternario, oltre agli Atti ufficiali del C.G.I., le Newsletters della I.A.G. e le relazioni delle campagne glaciologiche annuali. Dal 1988 vengono pubblicati anche volumi tematici, che raccolgono lavori su argomenti specifici, atti di congressi e simposi, monografie regionali sotto la denominazione «Geografia Fisica e Dinamica Quaternaria - Supplementi». La lingua usata dalla rivista è l'Inglese, ma gli articoli possono essere scritti anche nelle altre principali lingue scientifiche.

Editor Emeritus (*Direttore Emerito*)
P.R. FEDERICI
Dipartimento di Scienze della Terra, Via S. Maria 53 - 56126 Pisa - Italia - Tel. 0502215700

Editor in Chief (*Direttore*)
C. BARONI
Dipartimento di Scienze della Terra, Via S. Maria 53 - 56126 Pisa - Italia - Tel 0502215731

Vice Editor (*Vice Direttore*)
A. RIBOLINI
Dipartimento di Scienze della Terra, Via S. Maria 53 - 56126 Pisa - Italia - Tel 0502215769

Editorial Board (*Comitato di Redazione*) **2020**

F. ANDRÈ (Clermont Ferrand), D. CAPOLONGO (Bari), L. CARTURAN (Padova), A. CENDRERO (Santander), M. FREZZOTTI (Roma), E. FUACHE (Paris/Abu Dabi), E. JAQUE (Concepcion), H. KERSHNER (Innsbruck), E. LUPIA PALMIERI (Roma), G. MASTRONUZZI (Bari), B. REA (Aberdeen), M. SCHIATTARELLA (Potenza), M. SOLDATI (Modena e Reggio Emilia).

INDEXED/ABSTRACTED IN: Bibliography & Index of Geology (GeoRef); GeoArchive (Geosystem); GEOBASE (Elsevier); *Geographical Abstract*: *Physical Geography* (Elsevier); GeoRef; Geotitles (Geosystem); Hydrotitles and Hydrology Infobase (Geosystem); Referativnyi Zhurnal.
Geografia Fisica e Dinamica Quaternaria has been included in the Thomson ISI database beginning with volume 30 (1) 2007 and now appears in the Web of Science, including the Science Citation Index Expanded (SCIE), as well as the ISI Alerting Services.

HOME PAGE: http://gfdq.glaciologia.it/ - CONTACT: gfdq@dst.unipi.it

Printed with the financial support from (pubblicazione realizzata con il contributo finanziario di):

- Comitato Glaciologico Italiano
- Associazione Italiana di Geografia Fisica e Geomorfologia
- Ministero dell'Istruzione, Università e Ricerca
- Consiglio Nazionale delle Ricerche
- Club Alpino Italiano

Comitato Glaciologico Italiano
President (*Presidente*) M. FREZZOTTI

Geogr. Fis. Dinam. Quat.
43 (2020). 209-220, 7 figg., 4 tabb.

DOI 10.4461/ GFDQ.2020.43.9

Guillermo TAMBURINI BELIVEAU [1*] & Gioachino ROBERTI [2]

HIGH RESOLUTION SPOT DEM OVER LARGE AREAS IN CENTRAL AND SOUTH ANDES AND OBSERVATIONS ON THE 2018 PERITO MORENO GLACIAL LAKE OUTBURST FLOOD

Abstract: Tamburini Beliveau G. & Roberti G., *High resolution SPOT DEM over large areas in central and south Andes and observations on the 2018 Perito Moreno glacial lake outburst flood.* (IT ISSN 0391-9839, 2020).

This study describes the use of multi-temporal SPOT 6 and 7 tri-stereo images for producing high resolution (3 × 3 m pixel) digital elevation models (DEM) over two large (2680 and 837 km²) mountainous and glaciated regions in the Argentinian Andes. The images were radiometrically adjusted to enhance matching over different light intensity conditions, allowing for photogrammetric reconstruction in zones of both poor texture and chromatic contrast. Independent point clouds were obtained from every image pair and contrast adjustment, and then merged into a single point cloud, which was cleaned from noisy points by an iterative filtering process. The first testing place, the Cordón de la Ramada massif, is in the Central Andes, an arid area with one of the highest density of rock glaciers in the world and some of the highest peaks of the Americas. The second is in the Parque Nacional Los Glaciares in the Southern Andes, host of the notorious Perito Moreno glacier which ends in the Lago Argentino, forming cyclical ice-dams with a consequent downstream flooding after dam-break. This work provides 1) a practical application to generate high resolution DEM from SPOT 6 and 7 tri-stereo images, 2) the first high resolution DEM over Cordón de la Ramada and Perito Moreno glacier, and 3) the March 2018 pre- and post- ice-dam break DEM for the Perito Moreno glacier, which provides the opportunity to describe this glacial lake outburst flood.

Key words: SPOT satellites, Digital elevation model, Glacial lake outburst flood, Andean glaciers.

Riassunto: Tamburini Beliveau G. & Roberti G., *SPOT DEM di alta risoluzione di vaste aree nelle Ande centrali e meridionali e osservazioni sull'esondazione del lago glaciale del Perito Moreno nel 2018.* (IT ISSN 0391-9839, 2020).

Questo studio illustra l'utilizzo di immagini tri-stereo multi-temporali SPOT 6 e 7 per modelli altimetrici digitali (DEM) di alta risoluzione (3 × 3 m pixel) di due vaste regioni (2680 e 837 km²) montuose glacializzate nelle Ande argentine. Le immagini sono state radiometricamente modificate per incrementare le corrispondenze fra punti in diverse condizioni di intensità di luce, rendendo possibile una ricostruzione fotogrammetrica in zone di scarso contrasto sia di tessitura che cromatico. Sono state ottenute nuvole di punti indipendenti per ogni coppia di immagini e modifica di contrasto, poi successivamente unite in un'unica nuvola di punti dalla quale sono stati eliminati punti erroneamente proiettati attraverso un processo di filtraggio iterativo. La prima area test, il Cordón de la Ramada, si trova nelle Ande centrali, e consiste in un'area arida con una delle più alte densità di rock glacier nel mondo, oltre alla presenza delle cime più alte delle Americhe. La seconda area test è collocata nel "Parque Nacional Los Glaciares" nelle Ande Meridionali, dove si trova il famoso Ghiacciaio Perito Moreno che termina nel Lago Argentino formando sbarramenti temporanei e conseguenti onde di piena a seguito del loro collasso. Questo lavoro fornisce a) un'applicazione pratica per la generazione di DEM ad alta risoluzione da immagini tri-stereo SPOT 6 e 7, b) il primo DEM di alta risoluzione del Cordón de la Ramada e del Ghiacciaio Perito Moreno e c) i DEM del Marzo 2018, pre e post collasso dello sbarramento glaciale del Perito Moreno, fornendo elementi utili per descrivere il fenomeno di esondazione che ne è conseguito.

Termini chiave: Satelliti SPOT, Modelli altimetrici digitali, Esondazioni laghi glaciali, Ghiacciai andini.

INTRODUCTION

In this study, we present a workflow to produce high resolution DEM (3 m pixel) over large areas using "Satellite Pour l'Observation de la Terre" (SPOT) 6 and 7 tri-stereo images. The same workflow has been partially followed by Tamburini Beliveau (2018) to study high mountain glacial environments in Argentinian Central Andes.

The SPOT program was started in 1986 by the CNES (Centre National d'Études Spatiales, the national space agency of France) and is one of the longest standing civilian and commercial earth observation programs which offers some of the optical highest spatial resolution imag-

---

[1] *CIT Santa Cruz - CONICET, Santa Cruz, Argentina.*
[2] *Independent researcher, Squamish, BC, Canada.*
[*] *Corresponding author: G. Tamburni Beliveau (guitambe@fceia.unr.edu.ar)*

The scenes used in this study were made available thanks to an agreement between the researchers and the CONAE. We are also thankful to Carolina Mirallas of the LaIC (Laboratorio de Inglés Científico) for the language support. We would also like to thank A. Rivera and A. Cevallos for apporting two GCP on the Cerro Mercedario peak, and to Aonikenk Tehuelche for her studies of the important Santa Cruz River before it soon disappears under two big dams.

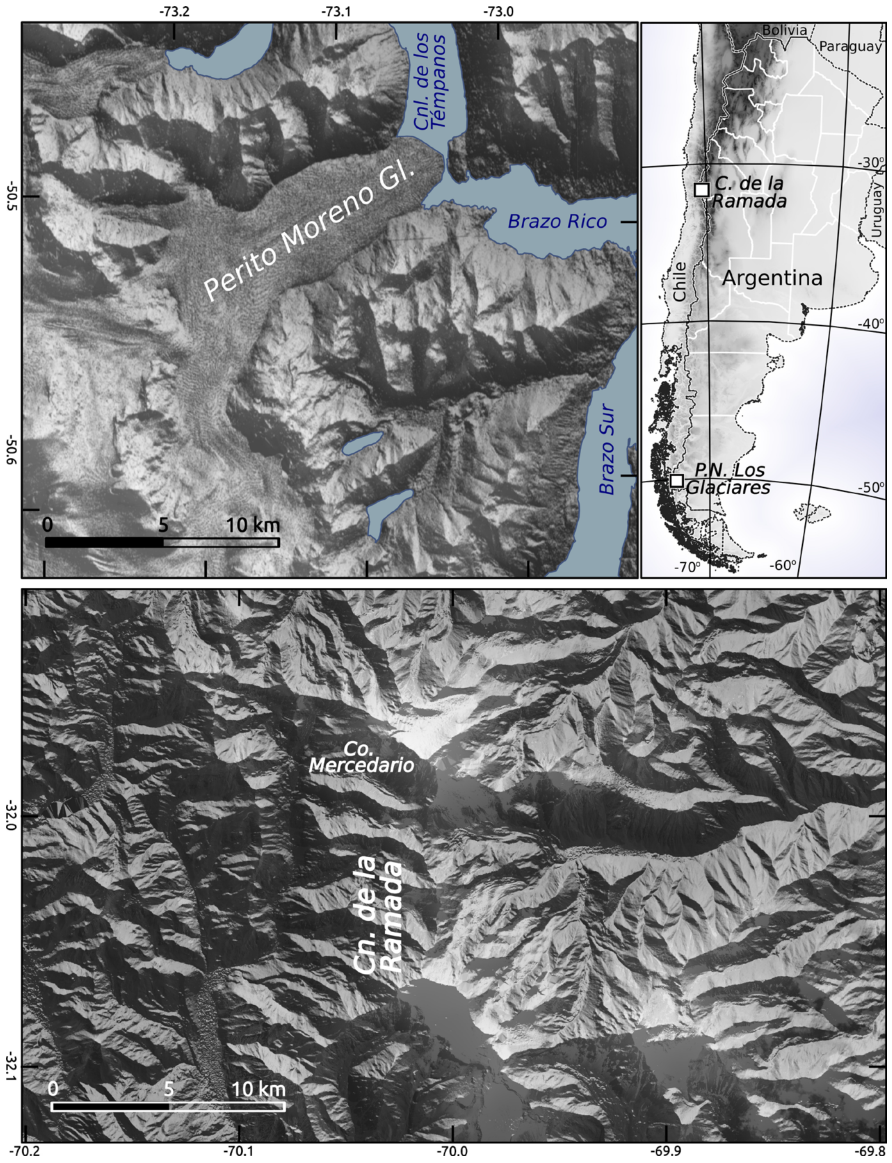

FIG. 1 - Location of the study areas. White squares on the general map (top right) represent an area of 10,000 km² . Resulting DEM visualizations (top left and bottom) with a composite of a hillshade map and the orthophoto with different levels of transparency.

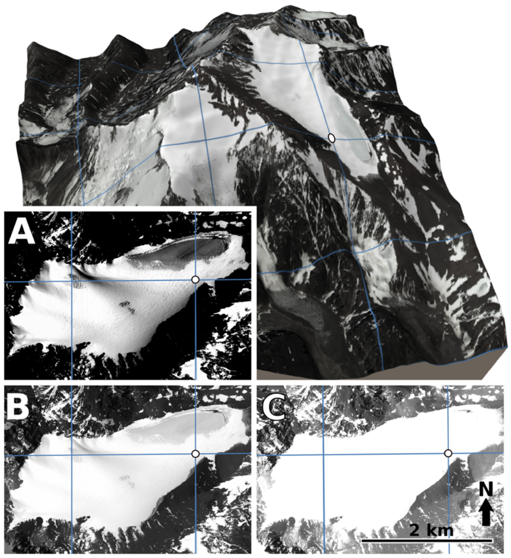

FIG. 2 - Cerro Mercedario in the Cordón de la Ramada DEM, and its two main glaciers: La Hoyada and El Caballito (derived SPOT orthophoto superimposed). In detail, three views of the La Hoyada glacier (white dot at 31.96° South, 70.10° West, grid spacing 0.02) showing the three different radiometric adjustments to enhance matching over A) overexposed, B) medium exposition and C) underexposed areas.

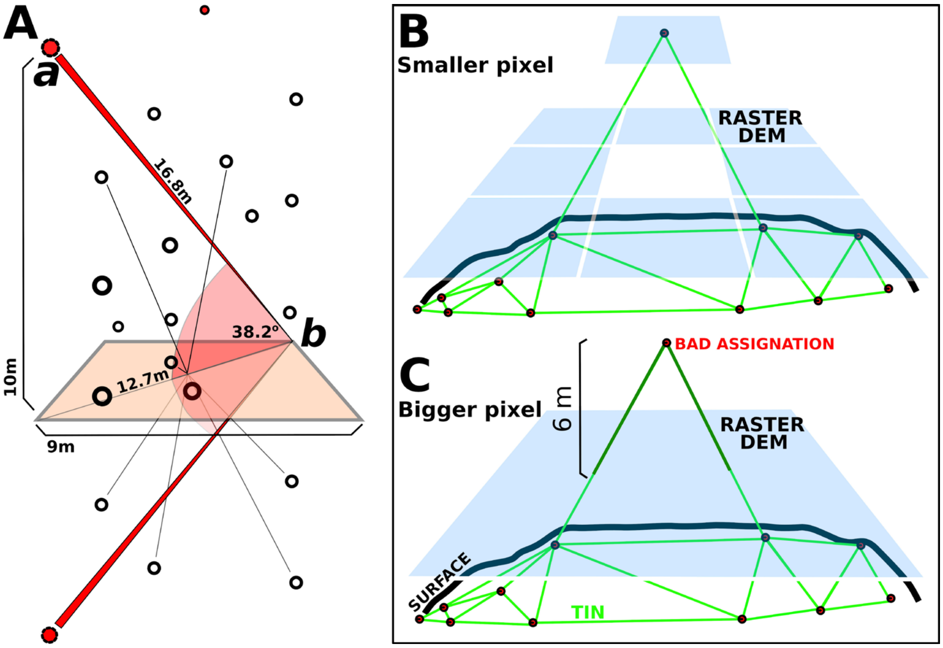

Fig. 3 - A) DEM filtering criteria used in the first iteration. Successive iterations follow the same approach but using different parameters. The red dots correspond to the points eliminated in the cloud. B) and C) represent the filtering criteria in the final step (6, iteration 2), used to filter outliers in areas with low contrast (snow/water) where only few points may be found in a large area. Increasing the pixel size of the reference DEM helps to reduce sensitivity to outliers in these regions.

es (Leprince & *alii*, 2007; Poli, 2005). The quality of this data is exceptional due to the robustness and stability of the orbital system, the wide dynamic range and the unique format of simultaneous acquisition of three stereoscopic images (stereo triplet) (Perko & *alii*, 2019; Alganci & *alii*, 2018; Gaddam & *alii*, 2019).

Exploiting these multiple technical benefits, we show how to deal with two challenges in the automatic point cloud generation process: 1) to carry out image matching in underexposed and overexposed zones of the satellite images: e.g. forested areas shadowed by the mountains and clean and flat ice respectively; and 2) filtering and removal of wrongly extracted points resulting from bad assignations in the mass point generation process. By modifying image histogram and contrast, we were able to obtain much denser point clouds than by just following standard workflows that do not account for image lighting conditions. Additionally, by filtering the final point cloud through a guided iterative procedure, we were able to dramatically reduce noise in the results.

We worked over two mountainous and glaciated regions: the Cordón de la Ramada (Tamburini Beliveau, 2018) and the Perito Moreno Glacier valley (Lodolo & *alii*, 2020). Two sets of satellite stereo-triplets were acquired a few weeks apart from each other for each study area. We produced four main independent point clouds, two for each location. These results were combined in the Cordón de la Ramada to obtain a more detailed DEM, and we partially kept the Perito Moreno Glacier point clouds separate to identify pre- and post- ice-dam morphology and the glacial lake outburst flood (GLOF) of March 11th 2018. This work demonstrates the potential of the SPOT last generation sensor for high resolution DEM generation over large areas.

STUDY AREAS

The two study areas are glaciated terrains in the Andes (fig. 1). The first area is about 2680 km² (67 × 40 km) at 32° latitude South 70° longitude West, over the Argentinian Central Andes in the Cordón de la Ramada massif. This massif houses the Cerro Mercedario (see fig. 2) which is 6770 m asl and it is the 4th highest peak in the Andes, located 65 km north of the Aconcagua peak, the highest of the western and southern hemispheres. This high mountainous area is characterized by extreme aridity, in which only small and slow-moving glaciers can develop. However, a widespread development of periglacial conditions favours the formation of rock glaciers (Villarroel & *alii*, 2018), making it one of the regions of the world with the highest density of rock glaciers (Trombotto & *alii*, 1997; Schrott, 1991).

The second area encompasses 837 km² (31 × 27 km), at 50° latitude South and 73° longitude West. This area includes the Perito Moreno glacier (figs. 5, 6) in the Parque Nacional Los Glaciares, located in the subantartic ecoregion of the Patagonian Woods in the southern Andes (Morello & *alii*, 2012). Very differently from Cordón de la Ramada, this is one of the wettest areas on the planet, having over 2500 mm of mean annual rainfall (NASA, 2020; Millan & *alii*, 2019) (fig. 1). The Perito Moreno glacier is 23 km long, and covers an area of 200 km². It is a temperate valley glacier which flows from the Southern Patagonian Ice Field, the largest ice mass in the Southern Hemisphere outside Antarctica (Millan & *alii* 2019). Perito Moreno calves in the deep Lago Argentino (150 m deep in average and maximum depths greater than 600 m) and periodically, but not regularly, dams one of its main branches, the Brazo Rico (Lenzano & *alii*, 2014). The ice dam causes the rise of the water level until it breaks and suddenly releases the accumulated water, causing downstream flooding in a clear example of a glacial lake outburst flood.

METHODS

We processed two different stereoscopic triplets in each of the two study areas with a time gap between scene acquisitions of two months for the Cordón de la Ramada, and one month for the Perito Moreno Glacier. The four sets of tri-stereo satellite images were processed with ERDAS Imagine 2014 (the former Leica Photogrammetry Suite, LPS) (Intergraph, 2013), a state-of-the-art software toolbox for the 3D photogrammetric reconstruction and point cloud generation. We used ERDAS because of its proven versatility and rigorous photogrammetric reconstruction algorithm (Gaddam & *alii*, 2019; Mészáros & *alii*, 2008; Lamsal & *alii*, 2011). ERDAS enables the user to choose the most suitable photogrammetric algorithm, and to automatically load the internal orientation (IOP) and external orientation (OEP) parameters. The software package supports detailed processing report export.

We followed the standard ERDAS photogrammetric workflow for the DEM generation (Intergraph, 2013), with some modifications to enable matching in underexposed and overexposed scenes and filtering wrongly extracted points in the clouds (fig. 3). Point cloud filtering to improve DEM quality and final 2D and 3D graphical representations of the DEM were performed in Geographical Information Systems (GIS) software. A differential GPS field campaign was carried out in the Cordón de la Ramada to collect high precision ground control points (GCP) to check the DEM accuracy. The field campaign at Perito Moreno Glacier was cancelled due to the COVID-19 pandemic.

We worked with SPOT 6 and 7 satellite scenes with tri-stereo characteristics acquired by the SPOT orbital pushbroom sensor and stored as Pleiades DIMAP .xml format. The nominal spatial resolution of the sensor is 1.5 m and the radiometric one is 12-bit panchromatic, representing 4096 levels of grey in the wavelength of the visible spectrum. The principal characteristics of SPOT 6 and 7 optical sensors are presented in Table 1, and Table 2 shows the details of the processed image.

Point cloud generation

To obtain final raster DEM from the SPOT scenes, we first reconstructed the point clouds in ERDAS (Intergraph, 2013). Then, the estimated outlier points were filtered, and the resulting clouds were interpolated to a TIN and saved as a raster.

As a first step of the processing, we modified the scenes histogram to enhance mass points matching in low contrast areas and the filtering step was iterated three times to get cleaner results. The whole workflow is presented in fig. 4 and described below.

- Step 1 in fig. 4. Image histogram editing to improve matching in areas of low radiometric contrast:

We observed that the algorithm for the correlation and identification of correlative points (mass points) for point cloud calculation between image pairs in ERDAS performs poorly in areas of low radiometric contrast. A radiometric adjustment was made to solve this problem. Radiometric values (pixel digital numbers) are distributed in a histogram where the most frequent values are close to a peak of a histogram curve. Commonly, image digital numbers are – by default – rendered in the colour scale in proportionally constant intervals in the absolute range of digital numbers (Gonzalez & Woods, 2018). In that case, homogeneous areas on the surface with scarce variation of the pixel digital numbers show low contrast when visualizing, which therefore perform poorly in the automated point cloud extraction.

In order to solve this problem, the intensity scale was divided into three sectors: dark, medium and clear. Three independent copies of the images were created with modified histograms to better adapt to overexposed and underexposed areas and to take advantage of the full radiometric scale of the images. The histograms were enhanced with the standard deviation method (2.0 standard deviation stretch, Gonzalez & Woods, 2018). First, the most critical areas were considered: shadows and woods in the dark regions, flat ice and snow in the clear ones, and bare rock surfaces, moraines and other sediments in the medium tones. The histograms were stretched to obtain optimal contrast in those areas selecting a representative sampling area. Then, the same parameters that were applied for the modification of the histogram in the sampling area of interest were applied to the pixel digital number curve of the entire image, enhancing then the areas of interest in the whole scene (Intergraph, 2013).

As a consequence, three different optimally adapted datasets were obtained to represent dark (underexposed), medium (central tones) and clear (overexposed) areas in each case (see figs 2A, B, C, and 5A, B). Modified images were rescaled and stored as 8-bit greyscale files, and three projects were set consisting exactly of the same configuration, except for the substitution of the radiometrically rescaled images to produce dense point clouds over the critical areas.

- Step 2 in fig. 4. Photogrammetric block definition, configuration of camera parameters and image import:

For the photogrammetric block adjustment model, the default physical pushbroom SPOT-sensor model was used to fully exploit the detailed sensor metadata. The precise camera IOP and EOP were automatically imported from the scene metadata files[1]. Six images (two stereo triplets in two different capture dates for each area) were loaded in each photogrammetric block. The project was defined in Geographic WGS84 reference system with ellipsoidal heights.

- Step 3 in fig. 4. Aerial triangulation configuration and point cloud generation:

For the Cordón de la Ramada, GCP and checkpoints (CP) were added to the project, selecting only those that could be identified with pixel precision in the images. For the Perito Moreno area, all information was processed over the very detailed EOP, except for one GCP (code: GERO). This point is sited in a flat zone and it was not possible to identify its precise planimetric position in the images at one pixel precision. However, given that it is located in a flat area, leaving a wide tolerance (around 3 pixel radius) with respect to the horizontal coordinates, does not affect the al-

TABLE 1 - Characteristics of SPOT 6 and 7 optical sensors. Adapted from European Space Agency (2020); Coeurdevey & Fernandez (2019).

SPOT 6 and 7 sensor characteristics	
Camera type	Orbital, telescope Korshc. Pancromatic.
Sensor type	linear pushbroom
Focal length	3760.36 mm
Aperture	200 mm
Sensor columns	28000
Pixel size on image	8.3372 μ
Pan. spectral band	0.450-0.745 mm
Flight height	694 km
Instantaneous field of view	30°
Viewing angle between consecutive images	15-20°
B/H ratio stereo pair	0.27-0.4
Swath	60 km at nadir
Ground sampling distance (nadir)	2.2 m
Spatial resolution on ground (resampled)	1.5 m
Radiometric resolution	12 bits

TABLE 2 - SPOT 6 and 7 products used in this work.

SPOT 6 and 7 project datasets		
SPOT triplets. Product ID	Date and time	Image Centre Location
Cordón de la Ramada		
SPOT7_20160101_143016500 SPOT6_20160308_141737800	2016-01-01 14:30:16 2016-03-08 14:17:37	S032°00'03" W070°04'33" S032°00'06" W070°04'36"
Perito Moreno		
SPOT7_20180214_142623800 SPOT6_20180320_141437600	2018-02-14 14:26:23 2018-03-20 14:14:37	S050°26'40" W073°18'18" S050°38'52" W073°18'21"

timetric value of the point. This point is from the Argentinian national positioning and levelling network; its position in the scenes was determined from an analysis of technical reports (Gillone & Brunini, 1998; Instituto Geográfico Nacional, 2020).

Approximately 100 tie points per 1000 km² were automatically identified. Residuals of the tie points calculation were observed in the photogrammetric block adjustment triangulation report to identify the wrongly assigned ones (i.e., the tie points with large residuals). The tie points have to correspond to the same element in every image, and consequently, to the same a priori coordinates on the ground. Points with high residuals (> 5 m) were manually located and observed in the scenes to verify that they effectively corresponded to bad assignations. In those cases, the tie points were eliminated and new tie points were manually added to compensate for the eliminated ones. Finally, triangulation was performed again.

With the adjusted block and a favourable triangulation report, the point cloud was generated.

In the photogrammetric processing, every stereo-pair of each triplet gives as a result one point cloud. So, every dataset gave three point clouds (being the images of the triplet A, B, and C, the resulting point clouds would be A-B, A-C, and B-C). As the datasets were replicated with three different radiometric adjustments (processed in independent projects), we finally obtained nine independent point clouds for each of the four dataset (two satellite acquisitions over two areas).

Point cloud editing

Once the point clouds in ERDAS were obtained, they were post-processed in an iterative filtering procedure to delete wrongly assigned mass points and to export final raster DEM in a GIS environment. The applied filtering concept relies on comparing the point cloud with a smoothed version of the raster DEM derived from the very same point cloud, identifying and removing points too far from the smoothed surface. The iteration was performed with an empirical incremental filtering criteria to identify the wrongly extracted mass points.

Three GIS softwares (QGIS, SAGA and Global Mapper, Conrad & *alii* (2015); Quantum GIS Development Team (2020); Blue Marble Geographics, 2020), were used at different stages of the post-processing and complemented with Inkscape (Inkscape, 2020) design drawing software for the final cartographic representations.

- Step 4 in Workflow fig. 4, iteration 0:

– Global Mapper (4.1): The nine point clouds for every tri-stereo dataset were merged and a TIN was saved as raster DEM file. A high frequency/low amplitude noise was observed in the TIN as small peaks apart from the mean surface, clearly visible in the shaded representation of the DEM (black arrows on fig. 5C). A first smoothing of the raster DEM was obtained by setting it at 9 × 9 m, nine times larger than the default resolution considering the point density of the cloud (3 × 3 m).

– SAGA (4.2): Smoothed raster DEM values z from previous step were assigned to all points in the point cloud (new column in the vector file: DEM z) for further calculation (DEM value of the pixel intersected by the vertical projection of the point in the cloud).

– QGIS (4.3): To identify and delete outliers (high frequency/low amplitude noise), we computed the absolute vertical difference between the original z coordinate of each point in the cloud and the corresponding pixel value z in the interpolated and smoothed raster DEM. Points with absolute difference > 10 m from the interpolated

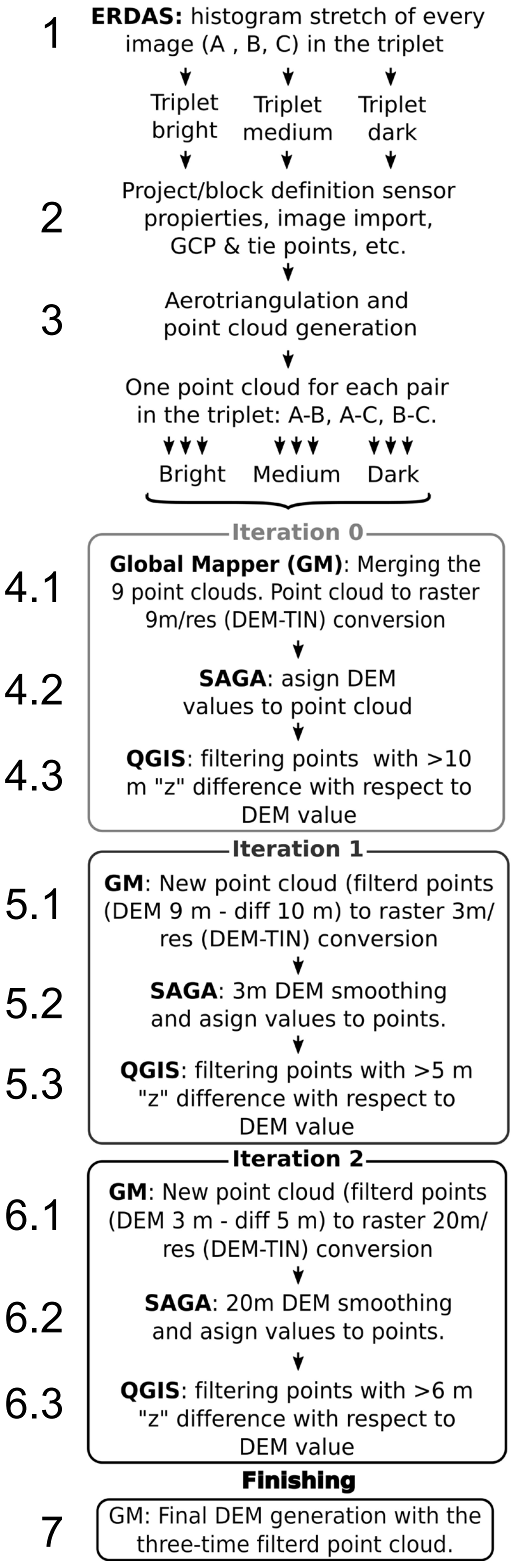

FIG. 4 - Schematic representation of the workflow followed in this study.

DEM were eliminated as they most likely represent photogrammetric reconstruction outliers generated by incorrect matching during ERDAS calculation (false positives). We selected a 10 m vertical difference threshold with the following empirical approach.

One could draw a hypothetical line joining a point of the cloud 10 m distant of a pixel corner of the DEM to the opposite corner of the very same pixel, *a* and *b* in fig. 3A respectively. On one hand, the line corresponding to this geometrical configuration represents a ground slope of about 38.2° (78.5%), being it the slowest slope value that will be eliminated when applying the filter. This value, contrasted to independent sources (SRTM DEM, Farr & *alii*, 2007), is over the mean slope in the area which is 33° excluding flat terrain, i.e. valley bottoms and water surfaces. And, on the other hand, this geometrical configuration is very unlikely to happen. So, we consider the filter adequate because there will be very few cases of false negatives (i. e., eliminated points when they are in fact locations on the ground), as all eliminated points belongs to a set of points which are at the same time far from the mean surface and from the mean slope values (see fig. 3A).

– After merging and filtering, a new point cloud was generated.

- Step 5 in Workflow fig. 4, iteration 1:

– Global Mapper (5.1): The resulting filtered point cloud was then re-interpolated at full resolution into a 3 × 3 m pixel raster DEM. Still observing a residual high frequency/low amplitude noise (see fig. 5C, D) we repeated the steps of iteration 0 but with finner configuration values.

– SAGA (5.2): Seeking to better preserve the surface shapes, the 3 × 3 m raster DEM was smoothed instead than resampled to lower resolution as in iteration 0. A 3 pixel window Gaussian filter at one standard deviation was applied, and values from the new DEM were assigned to the points of the new point cloud in a new data column.

– QGIS (5.3): Next, we eliminated points with > 5 m absolute vertical difference with respect to the new smoothed DEM of 3 × 3 m pixel.

– A new cleaner point cloud was generated.

- Step 6 in Workflow fig. 4, iteration 2:

– Global Mapper (6.1): In the raster resulting from Iteration 1, a low frequency/high amplitude noise still persisted. Outliers isolated in areas with very low density of mass points (for example flat snowed surfaces with almost null contrast) revealed as high peaks or deep holes in the shadowed DEM. To eliminate these outliers, a new DEM was interpolated at 20 m and Gaussian filter of radius two and one standard deviation: this is equivalent to one point in 20 × 20 m, 44 times less points than at full resolution (see fig. 3B, C, and results Section 3). In these cases, in which the point cloud was sparse, even with the lower resolution/smoothed DEM interpolation, the outliers remained too close to the DEM surface because they were the only points which had been represented in a large area. Thus, the raster interpolation tended to the proximity of that isolated reference.

– SAGA (6.2): Smoothed DEM values were assigned to points in the new point cloud.

– QGIS (6.3): After performing a visual evaluation, we decided to eliminate points with an absolute difference > 6 m.

- Step 7 in Workflow fig. 4, final raster:

– Global Mapper (7): The final raster DEM was created by TIN interpolation in Global Mapper with the third filtered point cloud at default resolution of 3 × 3 m pixel.

A different approach needed to be taken for point cloud interpolation into raster DEM at the front of the Perito Moreno Glacier. In this area, there is an interpolation problem between the points on the shore of the lake and those in the front of the glacier. This front is a calving vertical wall of ice, up to 70 m high above the surface of the lake water. Because the observation angle of the satellite telescope is not nadiral, and it is not possible to obtain mass points on the surface of the water, the rendering of the interpolation represented a sloping surface from the shoreline to the upper sector of the glacier front, as shown in fig. 5C. To avoid this problem, points with a z value equal to that of the lake water level were manually incorporated into the perimeter of the glacier front for a correct interpolation, fig. 5D.

DEM validation

A field GPS campaign to validate the Perito Moreno Glacier DEM was planned for the southern summer-autumn 2020. However, this campaign had to be cancelled due to the COVID-19 pandemic. To check the DEM quality, we then used the results of validation campaigns carried out for the Cordón de la Ramada DEM in different periods between 2014 and 2016 for the Tamburini Beliveau (2018) PhD research.

In these initial campaigns, precise locations of 30 GCP were determined with dual-frequency GPS field measurements (See Table 3). Final coordinates in ITRF08 (2016) with ellipsoidal heights were obtained with the Precise Point Positioning (PPP) scheme processing offered by the Natural Resources Canada online service (Bisnath & Collins, 2012; Natural Resources Canada, 2020). In four cases, GCP were double checked against geodetic vertices of the Argentinian PASMA mining network (Instituto Geográfico Nacional, 2020). The precision obtained with the PPP processing was between 0.15 and 0.30 m in planimetry and altimetry, respectively, which is sufficient to validate the 3 × 3 m resolution DEM (Tamburini Beliveau, 2018). Two GCP, MERC (2006) and CEV (1997) had been taken several years earlier at more than 6700 m asl and could not accurately be identified on the photographs. The CEV point was also taken with a simple frequency instrument in WGS72 (transformed to ITRF08), making the precise adjustment to the current reference system more difficult. However, MERC and CEV were included as altimetric references as they were the only sources to check the DEM at very high altitudes.

Standard deviation in elevation difference between GCP and DEM is 2.79 m. One point (GCP 7) was excluded from the error estimation because it showed higher residuals, probably due to some gross error which has not been identified.

Table 3 - GCP for the Cordón de la Ramada DEM. Coordinates with ellipsoidal height (h) ITRS and the difference between the DEM coordinates (h-DEM) are shown. The last row shows the standard deviation of the differences (σ).

	Ground control points measured in the Cordón de la Ramada				
ID	Code	Latitude (°)	Longitude (°)	h (m)	h-DEM (m)
1	A	-31.93427264	-70.02281586	3699.842	0.90
2	COMUN-1	-31.96479381	-70.05829044	4387.865	3.42
3	D	-31.95850086	-70.05368622	4203.603	-0.01
4	E	-31.95183967	-70.04738681	3994.337	-3.99
5	COMUN-4	-31.95166297	-70.04811969	4020.589	0.62
6	C	-31.94145994	-70.02689011	3796.823	2.15
7	14-106	-31.89655117	-70.20474583	4001.771	11.53
8	COMUN-2	-31.90399531	-70.16546247	3832.462	1.60
9	COMUN-3	-31.91699803	-70.16861928	4009.036	-0.76
10	14-109	-31.90080628	-69.93916272	2257.769	1.46
11	S3_05	-31.96112306	-70.04940000	4242.472	0.03
12	S3_04	-31.95851028	-70.04881342	4160.898	-2.71
13	S3_03	-31.95555533	-70.04803300	4090.547	3.93
14	s3-x	-31.95019094	-70.03636111	3921.14	3.06
15	s3-x2	31.92844336	-70.02146764	3632.601	-0.80
16	s3_6_09	-31.96208914	-70.05242817	4276.775	0.14
17	s3_7_10	-31.96468314	-70.05372861	4322.533	1.26
18	s3_8_11	-31.96788292	-70.05985672	4455.065	7.35
19	s3_9_12	-31.96658506	-70.06069994	4434.394	0.79
20	s3_1_13	-31.96158481	-70.05629792	4280.582	2.00
21	s3_11_14	-31.95397875	-70.05067436	4061.158	-2.04
22	s3_12_15	-31.95280858	-70.04751633	4047.121	2.83
23	s3_13_16	-31.95170225	-70.04734583	3993.988	-2.00
24	s3_14_17	-31.94170586	-70.02688486	3795.336	1.07
25	s4_1_18	-31.90285192	-70.00195594	3174.995	-0.49
26	s4_2_19	-31.90389136	-70.00208539	3183.04	2.35
27	s4_3_20	-31.89355878	-69.97984219	3135.927	1.75
28	s4_4_21	-31.89308981	-69.97822583	3121.324	4.75
29	14_112	-32.11502000	-70.20934658	3206.754	-1.05
30	s4_5_22	-31.90543983	-69.93332867	2219.721	6.40
31	MERC	-31.95712557	-70.11312549	6025.900	7.34
32	CEV	-31.97926246	-70.11311963	6754.539	5.15
σ					2.79

The Perito Moreno glacier DEM is referenced only with respect to the z value as outlined in step 3 of the workflow. Even when it was not possible to collect independent GCP to validate the quality of the Perito Moreno DEM, we assume an accuracy in an absolute reference system similar to that of the Cordón de la Ramada. This is because the

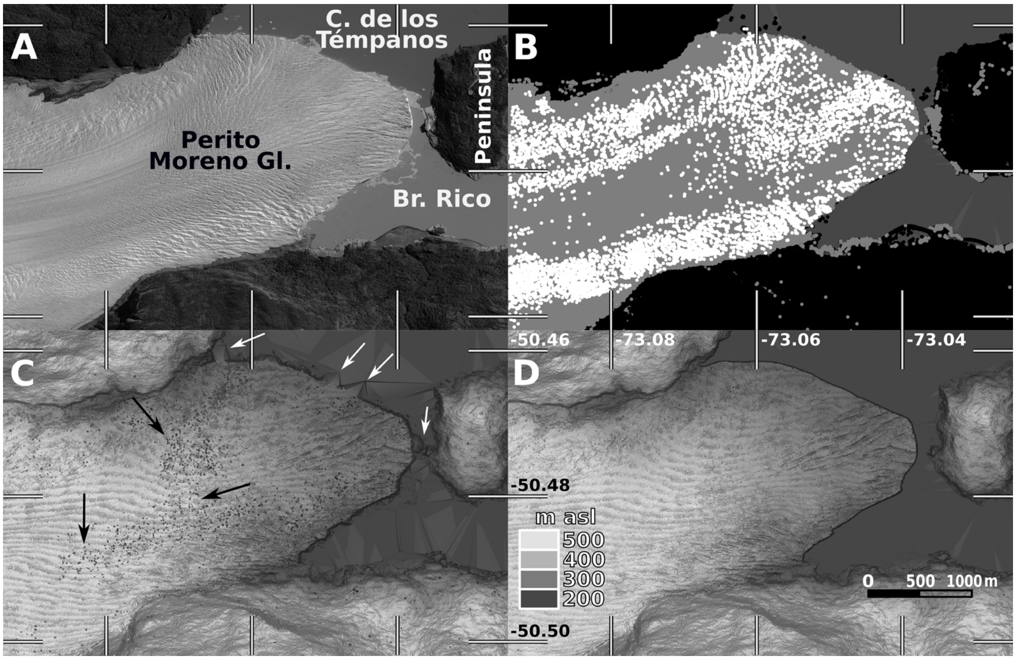

FIG. 5 - A) Ortophoto of the SPOT 6 scene at the Perito Moreno Glacier front acquired on 20th March. B) Three point clouds retrieved in this area: black dots are dark areas, grey are medium and white are light. C) Wrong interpolation (white arrows) and outliers (black arrows). D) Improved interpolation after filtering and manual point editing on the glacier front.

data and the workflow are the same. Accuracy in a relative coordinate system is, in both cases, at least equal to – and presumably better than – the absolute one. Table 3 shows the absolute difference and the standard deviation of the differences for each GCP with respect to the DEM of Cordón de la Ramada.

Processing system requirements

We used a Windows 7 virtual machine running on a Linux computer with 4 cores of a third-generation i7 processor and dedicated 6 GB of RAM. A minimum of forty minutes of processing per image pair over the 837 km^2 area was required. This processing time represents the best case scenario, after finding the optimal ERDAS configuration parameters through multiple trials with different settings.

RESULTS

The results of the processing are 4 DEM. Each DEM is the interpolation of a point cloud resulting from the merging of nine point clouds. Each point cloud has a point density of 1.3 million points per 1000 km^2, and the point cloud resulting from the merging has about 12 million points per 1000 km^2. The point cloud filtering steps reduced the total number of points to about 80% of the initial density, leading to an average point distribution of one point every 104 m^2, and a raster pixel of about 10 m resolution.

However, some areas have much denser point distribution than others, depending on the image contrast and texture (for example, areas covered by water do not have any points). On the other hand, when the chronologically independent final point clouds were merged, the point density doubled. The final raster DEM is sampled at 3 × 3 m, which is the best possible resolution at the areas with highest point cloud density. Visualizations of the most of the surface covered by the DEM are presented in fig. 1.

In the case of the Cordón de la Ramada, the two resulting DEM were merged into a single final DEM since the chronological difference between scenes was small and the surface changes were minimal.

In the case of the Perito Moreno Glacier, the two DEM were only partially merged. The point cloud resulting from SPOT 7 images was densified with those from SPOT 6 over stable areas where some of the SPOT 7 images were covered by clouds. The two DEM were kept separate over the glaciers for the observation of glacier dynamics, as presented in fig. 6.

TABLE 4 - SPOT 6 point cloud data for the Perito Moreno Glacier area.

SPOT 6 Perito Moreno number of points in point cloud (PC)			
PC Tone	Points in first combined PC	Points after third filtering iteration	% of original PC after filtering
Bright	2729457	2197501	80.51
Medium	4253715	3376582	79.38
Dark	2902900	2223599	76.60
Total of points	9886072	7797682	78.83

Observations on the Perito Moreno Glacier ice-dam break of 2018

We generated two DEM over the Perito Moreno Glacier area: one before and one after the ice-dam break that occurred in March 2018 (see fig. 6). Using these DEM, we traced the evolution of Perito Moreno ice-dam break, and here we describe the 2018 GLOF phenomena. This case study serves as an example of how satellite-derived DEM can help to prevent natural disasters (Mueting & *alii*, 2020; Zhou & *alii*, 2016).

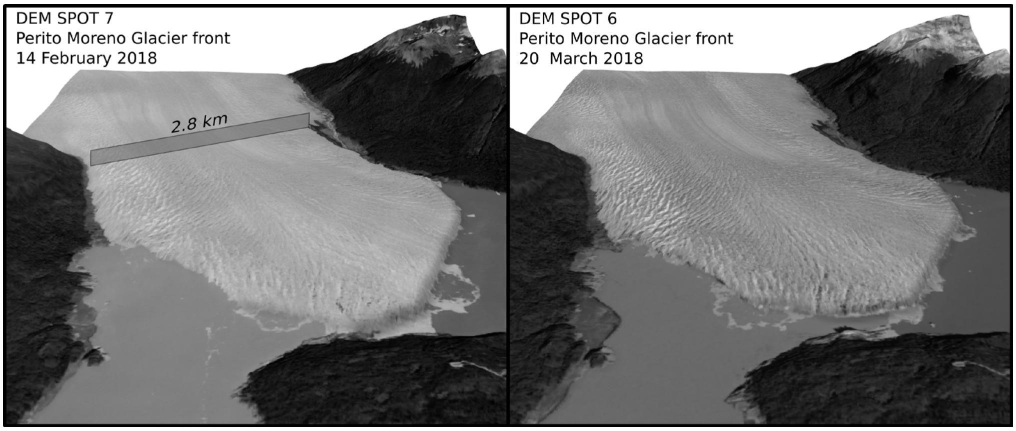

FIG. 6 - Perito Moreno Glacier front before and after the dam-break. Note the position of the ice front with respect to the peninsula and the two different tones of the water in the south and the north (left and right) due to higher sediment concentration of the water in the Brazo Rico (south).

The Perito Moreno Glacier calves into the Lago Argentino, the third biggest lake of South America (see fig. 1). The glacier calves in the strait between El Brazo Rico fresh water fjord and De los Témpanos channel, in front of the Peninsula de Magallanes. Periodically, but not regularly, with an average of 4.5 years in the 20th and 21th century, the glacier advances reaching the Peninsula de Magallanes and forming an ice-dam that closes the strait, the only connection between the Brazo Rico (and contiguous Brazo Sur) and the rest of the lake (Lannutti & *alii*, 2020; Millan & *alii*, 2019). When the ice-dam is present, the water in the closed fjord – now turned into an ice-dammed lake – rises with respect to the water level in the main body of the lake. The water level usually rises for a few months progressively flooding the surrounding lands until the hydraulic pressure starts to breach the ice-dam. Then, the water starts to filtrate the ice-dam through englacial and/or subglacial channels, gradually enlarging the ice fractures for a few days, until, in a few hours, the ice-dam eventually collapses. The sudden water release into the main body of the lake causes a GLOF that can partially flood the lake coastline.

Notable ice-dam events have occurred in the 20th century. In 1939, with a damming height of around 10.5 m, the ice-dam was bombarded by the Argentine Air Force in an attempt to mitigate the flood affecting farmlands around Brazo Rico, albeit without effective results (Lauricella, 2008). In 1954, the flooding of the Brazo Rico reached its highest level known to date, with 26 m (Stuefer, 1999). In 1988, the ice-dam reached one of the highest historical levels at 19 m. In this occasion, the dam break caused coastal flooding downstream, but at that time, El Calafate, the only town in the region sited in the shore of the lake, was still a small rural community and the town was not affected.

On the 11th of March of 2018, the dam broke. According to our SPOT DEM estimations with data from 25 days before the rupture and considering an increase in water level between 6 and 12 cm/day (Skvarca & Naruse, 2006), the water level in the Brazo Rico rose up to 14 ± 2.79 m at the moment of the rupture, the highest level since 1988. Taking into account that the area covered by the Brazo Rico and Sur is 117 km^2, the amount of water accumulated was about 1.5 km^3.

A day and a half after the ice-dam rupture, the Lago Argentino underwent an increase of 1.10 m in the water level over its 1350 km^2 (without the Brazo Rico and Brazo Sur) as a consequence of the sudden release of the water from the Brazo Rico and Sur (Ministerio de Obras Públicas, 2020). These values are equivalent to a release of 1.6 km^3 of water, 0.1 km^3 more than the estimate from the calculation of the increase of volume of water stored in the Brazo Rico.

The 0.1 km^3 difference between the volumetric values can be explained by the error margin in the measurements and/or by the water discharge of the large Santa Cruz river, which springs in the eastern side of the lake and drains to the Atlantic.

The ice-dam break caused partial flooding in the coastal area of the town El Calafate (fig. 7). El Calafate is nowadays an important touristic centre which has experienced recent urban growth. Such enlargement, however, has not been accompanied by careful urban planning. In particular, the possibility of coastal flooding due to ice-dam formation and braking has not been correctly assessed, resulting in about between 5 and 10 hectares of urban land inundated. The natural wild bird reserve of the wetlands of the Laguna Nimez and its facilities, contiguous to the coastal avenue in the village, were damaged as well. Additionally, the main coastal avenue and some squares were totally or partially flooded.

The adverse consequences of the floods were limited in other regions, since the surrounding area of the lake remains almost unoccupied. However, some touristic and scientific infrastructure (like docks, runways and paths, meteorological stations) in the National Park were affected by the floods of the outburst, and so were some of the belongings of the private owners who have occupation rights within the Parque Nacional Los Glaciares lands. The consequences of the GLOF were not catastrophic, but they were absolutely predictable both in the short and in the long terms. Observing human activities in the area, future GLOF of the Perito Moreno Glacier are not likely to generate dramatic scenarios. However, it is obvious that the consideration of the GLOF and of efficient spatial planning policies are crucial to avoid possible future damage. Technical tools such as this high resolution DEM can help to plan, predict and manage this type of situation.

FIG. 7 - A) Aerial and B) field views of the coastal flooding in Calafate following the Perito Moreno ice-dam failure (Tiempo Sur, 2018).

DISCUSSION

We showed how it is possible to produce a high quality DEM over large areas through the use of SPOT 6 and 7 data (Perko & *alii*, 2019; Kornus & *alii*, 2005; Alganci & *alii*, 2018) and their proven reliability. This was achieved by a simple and stable processing workflow in a user-friendly environment. The possibility of working entirely with free software tools was explored, but in the case of the photogrammetric software, we were not able to find a free software capable to correctly import all the image metadata, enable a full sensor model configuration and produce similar results in a relatively user friendly environment.

The whole workflow was possible without almost any type of manual editing of the data sets beyond the adjustment of parameter settings in the different software. Unique to the workflow presented in this paper are the facts that: A) each DEM is the combination of two stereoscopic datasets, and B) each DEM has been produced by merging different point clouds generated for three different radiometric brightness adjustments. This approach has improved our final results because by working with two stereo triples in the same area we obtain:

- Redundancy of ephemeris data and the adjustment parameters for the aereotriangulation calculation model. Being the same type of sensor and photogrammetric analytical model, it is possible to exploit this advantage.
- Full co-registration between the two sets by processing all the images together, which enables to increase resolution, or to compare the final results to analyze geomorphic changes in time.
- An increase in the quantity of mass points by incorporating more scenes with diversity of intensity values for the same locations. Even when only pairs from the same acquisition time were processed together, the combination of images of different dates allowed us to identify points thanks to smooth surface changes as, for example, the occurrence of light snow accumulation or changes in lighting conditions that distinguishes different features on the surface.
- An improvement in the detection of outliers, as independent datasets do not have correlation in non-systematic errors, and this gives higher weight to the resulting mean surface with respect to the outliers.

The previous considerations are valid for stable areas. In areas with intense surface changes, like the Perito Moreno Glacier surface or front in which changes are of meters per day (Ciappa & *alii*, 2010), the two point clouds need to be analyzed independently.

And in parallel, working with three different radiometric arrangements allowed us to dramatically increase the number of mass points in the automatic point cloud generation, exploiting the radiometric capabilities of the 12 bit grayscale sensor at a maximum and obtaining very good results over surfaces with shadows, ice, homogeneous sediment covers and low contrast in general (Toutin, 2006).

The iterative process to obtain the final point cloud by involving point filtering provides cleaner and less noisy data, although some information may be lost (see Table 4). Nearly 20% of the points were deleted for being considered false positives, but we can assume that some of them were real locations on the surface. The tradeoff between noise reduction in a single image and loss of detail is one of the classic bottlenecks in image processing (Casajus & *alii*, 2019; Gonzalez & Woods, 2018; Sarmiento & *alii*, 2019). Digital image processing or computing sciences provide different tools and theoretical approaches to manage different noise sources, such as low-pass or neighborhood filters (Casajus & *alii*, 2019; CloudCompare, 2020), which are usually more complex from a mathematical approach than the one we applied. In this work, by exploiting common software tools, we show a novel and practical approach by applying geomorphological constraints to filter point clouds and get a cleaner final DEM. Particularly, it proves very effective when retrieving real surfaces in areas with low density of points. In image processing in geosciences, it is common to have isolated reflector objects, like islands surrounded by water or rock outcrops in the middle of ice plates. In those cases, these objects would be the only surface reference in a wide area and eliminating them by filtering may reduce the quality of the final product. With our approach, these points remain preserved.

The product quality has been assessed from both visual evaluation and error analysis. The latter was evaluated by comparison between the resulting DEM and GCP coordinates in the Cordón de la Ramada. As a result, absolute vertical standard deviation between the DEM and the GCP is 2.79 m. Given that the DEM covers an area of almost 2680 km², and taking into account the data and the characteristics of the techniques (Alganci & *alii*, 2018), we estimate that our approach renders high accuracy suitable for geomorphic observations.

To conclude, SPOT products are not freely available and have a high economic cost. In this case, they were programmed and accessed at no cost under a research agreement signed with the CONAE (Comisión Nacional de Actividades Espaciales), the Argentine National Space Agency. CONAE allows free access to its satellite image catalogue for researchers from Argentine public institutions, but unfortunately it seems to be underused. Few pieces of work have taken advantage of these resources, least be said of their stereoscopic functionalities. Also attending to the access to the information and resources for high quality research, we consider that remote sensing field would be greatly enriched by the development of stable free photogrammetric software tools adapted for the agile processing of the data sources.

CONCLUSIONS

In this study, we presented a novel, relatively simple and systematic workflow to generate high resolution DEM over large areas with SPOT 6 and 7 tri-stereoscopic images, for which field work may be minimal or completely avoided. We showed how to perform a photogrammetic reconstruction in dark and bright areas by processing radiometrically adjusted images in separate projects, and how to improve point cloud quality by an iterative filtering and cleaning procedure. We then discussed how to georeference the DEM, even without high resolution GCP.

The final results are 3 × 3 m pixel DEM over 2680 km² in the Cordon de la Ramada and pre- and post- ice-dam DEM over 837 km² in the Perito Moreno Glacier, which make the procedure robust in different morphological and environmental challenging contexts. High resolution DEM can be used for multiple scientific and technical applications. We provide an example of the use of the DEM for describing the 2018 Perito Moreno GLOF and hence the possibility to improve land planning and hazard prevention nearby the glacier and along the coast of the Lago Argentino. Complementary to this, through this example we made a contribution in a subject of an increasing interest in the geosciences, which are glacial or landslide lake outbursts and their associated hazards occurring each time with a higher frequency in the current global warming context.

Notes

[1] In order to load the SPOT 7 scenes, whose format is identical to that of SPOT 6, we had to modify a line in the metadata .xml file by replacing the word "SPOT7" with "SPOT6" because of an unexpected error in that version of the software.

REFERENCES

ALGANCI U., BESOL B. & SERTEL E. (2018) - *Accuracy assessment of different digital surface models.* ISPRS International Journal of Geo-Information, 7 (3), 114. doi: 10.3390/ijgi7030114

BISNATH S. & COLLINS P. (2012) - *Recent developments in precise point positioning. Geomatica*, 66 (2), 103-111. doi: 10.5623/cig2012-023

BLUE MARBLE GEOGRAPHICS (2020). *Global mapper software.* Available: https://www.bluemarblegeo.com/about-us/index.php [Accessed 25 July 2020].

CASAJUS P.H., RITSCHEL T. & ROPINSKI T. (2019) - *Total denoising: Unsupervised learning of 3d point cloud cleaning.* In: 2019 IEEE/CVF International Conference on Computer Vision (ICCV). IEEE. doi: 10.1109/iccv.2019.00014

CIAPPA A., PIETRANERA L. & BATTAZZA F. (2010) - *Perito Moreno glacier (argentina) flow estimation by COSMO SkyMed sequence of high-resolution SAR-x imagery.* Remote Sensing of Environment, 114 (9), 2088-2096. doi: 10.1016/j.rse.2010.04.014

CLOUDCOMPARE (2020) - *Cloudcompare version 2.6.1. user manual.* Available: http://www.cloudcompare.org/doc/qCC/CloudCompare%20v2. 6.1%20-%20User%20manual.pdf [Accessed 25 July 2020].

COEURDEVEY L. & FERNANDEZ K. (2019) - *Pléiades imagery user guide.* Technical report, Airbus Defence and Space Intelligence.

CONRAD O., BECHTEL B., BOCK M., DIETRICH H., FISCHER E., GERLITZ L., WEHBERG J., WICHMANN V. & BÖHNER J. (2015) - *System for automated geoscientific analyses (saga)* v. 2.1.4. Geoscientific Model Development, 8 (7), 1991-2007. Available: https://www.geosci-model-dev.net/8/1991/2015/ [Accessed 25 July 2020].

EUROPEAN SPACE AGENCY (2020) - *Spot-6 and spot-7 commercial imaging constellation.* Available: https://directory.eoportal.org/web/ eoportal/satellite-missions/s/spot-6-7 [Accessed 25 July 2020].

FARR T.G., ROSEN P.A., CARO E., CRIPPEN R., DUREN R., HENSLEY S., KOBRICK M., PALLER M., RODRIGUEZ E., ROTH L., SEAL D., SHAFFER S., SHIMADA J., UMLAND J., WERNER M., OSKIN M., BURBANK D. & ALSDORF D.E. (2007) - *The shuttle radar topography mission.* Reviews of Geophysics, 45 (2), RG2004. doi: 10.1029/2005RG000183

GADDAM V.K., KULKARNI A.V., BJORNSSON H., GULLAPALLI S. & BALLINA M. (2019) - *Applications of SPOT-7 tri-stereo imagery in deriving the surface topography and mass changes of glaciers in Indian Himalaya.* Geocarto International, 1-21. doi: 10.1080/10106049.2019.1648567 [Accessed 25 July 2020].

GILLONE R. & BRUNINI C. (1998) - *Echar una red grande: El proyecto de asistencia al sector minero argentino (pasma).* Geoconvergencia, 28-36.

GONZALEZ R.C. & WOODS R.E. (2018) - *Digital Image Processing.* Pearson.

INKSCAPE (2020) - *Inkscape software.* Available: https: //inkscape.org/ [Accessed 25 July 2020].

INSTITUTO GEOGRÁFICO NACIONAL (2020) - *Ign. posgar 07. herramientas de búsqueda.* Red. Technical report, Instituto Geográfico Nacional.

INTERGRAPH (2013) - ERDAS Field Guide. Intergraph Corporation.

KORNUS W., ALAMUS R., RUIZ A. & TALAYA J. (2005) - *Assessment of dem accuracy derived from spot-5 high resolution stereoscopic imagery.* In: 6th Geomatic Week.

LAMSAL D., SAWAGAKI T. & WATANABE T. (2011) - *Digital terrain modelling using corona and ALOS PRISM data to investigate the distal part of Imja glacier, Khumbu Himal, Nepal.* Journal of Mountain Science, 8 (3), 390-402. doi: 10.1007/s11629-011-2064-0

LANNUTTI E., LENZANO M., DURAND M., VECCHIO, A.L., MORAGUES S. & LENZANO L. (2020) - *Modelado numérico de las oscilaciones frontales y ocurrencia de formación de diques de hielo del glaciar Perito Moreno, Campo de Hielo Patagónico Sur.* Cuadernos de Investigación Geográfica, 46 (1), 251-284. doi: 10.18172/cig.4213

Lauricella V. (2008) - *El día que bombardearon el perito moreno.* La Nación.

Lenzano M.G., Lannutti E., Toth C.K., Lenzano L.E. & Lovecchio A. (2014) - *Assessment of ice-dam collapse by time-lapse photos at the Perito Moreno glacier, Argentina.* ISPRS - International Archives of the Photogrammetry, Remote Sensing and Spatial Information Sciences, 40 (1), 211-217. doi: 10.5194/isprsarchives-xl-1-211-2014

Leprince S., Ayoub F., Klinger Y. & Avouac J.P. (2007) - *Co-registration of optically sensed images and correlation (cosi-corr): An operational methodology for ground deformation measurements.* International Geoscience and Remote Sensing Symposium (IGARSS), 1943-1946.

Lodolo E., Donda F., Lozano J., Baradello L., Romeo R., Bran D.M. & Tassone A. (2020) - *The submerged footprint of Perito Moreno glacier.* Scientific Reports, 10, 16437. doi: 10.1038/s41598-020-73410-8

Millan R., Rignot E., Rivera A., Martineau V., Mouginot J., Zamora R., Uribe J., Lenzano G., Fleurian B.D., Li X., Gim Y. & Kirchner D. (2019) - *Ice thickness and bed elevation of the northern and southern patagonian icefields.* Geophysical Research Letters, 46 (12), 6626-6635. doi: 10.1029/2019gl082485

Ministerio de Obras Públicas (2020) - *Sistema nacional de información hídrica.* Technical report, Ministerio de Obras Públicas, Argentina. Available: https://snih.hidricosargentina.gob.ar/ [Accessed 25 July 2020].

Morello J., Matteucci S.D., Matteucci S.D., Rodriguez A.F., Silva A.F. & Silva M. (2012) - *Ecorregiones y complejos ecosistémicos argentinos.* Universidad de Buenos Aires Orientación Gráfica Editorial.

Mueting A., Bookhagen B. & Strecker M.R. (2020) - *Using high-resolution DEMs for debris flow detection based on topographic signatures: A case study in the Quebrada del Toro, NW Argentina.* EGU General Assembly 2020.

Mészáros M., Szatmári J., Tobak S. & Mucsi L. (2008) - *Extraction of digital surface models from CORONA satellite satellite stereo images.* Journal of Environmental Geography, 1 (1-2), 5-10.

NASA (2020) - Nasa earth observatory. Total rainfall. Available: https://earthobservatory.nasa.gov/global-maps/TRMM_3B43M [Accessed 25 July 2020].

Natural Resources Canada (2020) - *Natural resources Canada. Precise Point Positioning.* Available: https://webapp.geod.nrcan.gc.ca/geod/tools-outils/ppp.php [Accessed 25 July 2020].

Perko R., Raggam H. & Roth P.M. (2019) - *Mapping with pléiades– end-to-end workflow.* Remote Sensing, 11 (17), 2052.

Poli D. (2005) - *Modelling of spaceborne linear array sensors.* PhD thesis, Mitteilungen/Institut für Geodäsie und Photogrammetrie an der Eidgenössischen Technischen Hochschule Zürich.

Quantum GIS Development Team (2020) - Quantum GIS software. Available: http://qgis.org/en/site/about/index.html [Accessed 25 July 2020].

Sarmiento J.C., Bercero A.M., Jimenez D.L., Fernández J.C. & Garcia-Almirall P. (2019) - Filtering surfaces in surveys with multiple overlapping: Sagrada familia. IOP Conference Series: *Materials Science and Engineering*, 471, 082044. doi: 10.1088/1757-899x/471/8/082044

Schrott L. (1991) - Global solar radiation, soil temperature and permafrost in the central andes, argentina: A progress report. *Permafrost and Periglacial Processes*, 2 (1), 59-66. doi: 10.1002/ ppp.3430020110

Skvarca P. & Naruse R. (2006) - Overview of the ice-dam formation and collapse of glaciar perito moreno, southern patagonia, in 2003/04. *Journal of Glaciology*, 52 (178), 476-478. doi: 10.3189/172756506781828539

Stuefer M. (1999) - *Investigations on mass balance and dynamics of Moreno Glacier based on field measurements and satellite imagery.* PhD thesis, Universität Innsbruck.

Tamburini Beliveau G. (2018) - *Magnitudes y características de los procesos geodinámicos en el ambiente glacial y periglacial del Cordón de la Ramada (Andes Centrales argentinos) mediante técnicas de teledetección.* PhD thesis, Universidad Nacional de Rosario - FCEIA, Rosario. doi: 10.13140/RG.2.2.32084.24968/1

Tiempo Sur (2018) - *Imágenes de la inundación en el calafate desde el aire.* Tiempo Sur.

Toutin T. (2006) - *Generation of dsms from spot-5 in-track hrs and across-track hrg stereo data using spatiotriangulation and autocalibration.* ISPRS Journal of Photogrammetry and Remote Sensing, 60 (3), 170-181.

Trombotto D., Buk E. & Hernández J. (1997) - *Monitoring of mountain permafrost in the central Andes, Cordon del Plata, Mendoza, Argentina.* Permafrost and Periglacial Processes, 8 (1), 123-129.

Villarroel C., Beliveau G.T., Forte A., Monserrat O. & Morvillo M. (2018) - *Insar for a regional inventory of active rock glaciers in the dry andes mountains of argentina and Chile with sentinel-1 data.* Remote Sensing, 10 (10), 1588. doi: 10.3390/rs10101588

Zhou Y., Walker R.T., Hollingsworth J., Talebian M., Song X. & Parsons B. (2016) - *Coseismic and postseismic displacements from the 1978 m w 7.3 tabas-e-golshan earthquake in eastern Iran.* Earth and Planetary Science Letters, 452, 185-196.

(Ms. received 19 October 2020, accepted 9 February 2021)

Edizioni ETS
Palazzo Roncioni - Lungarno Mediceo, 16, I-56127 Pisa
info@edizioniets.com - www.edizioniets.com
Finito di stampare nel mese di marzo 2021